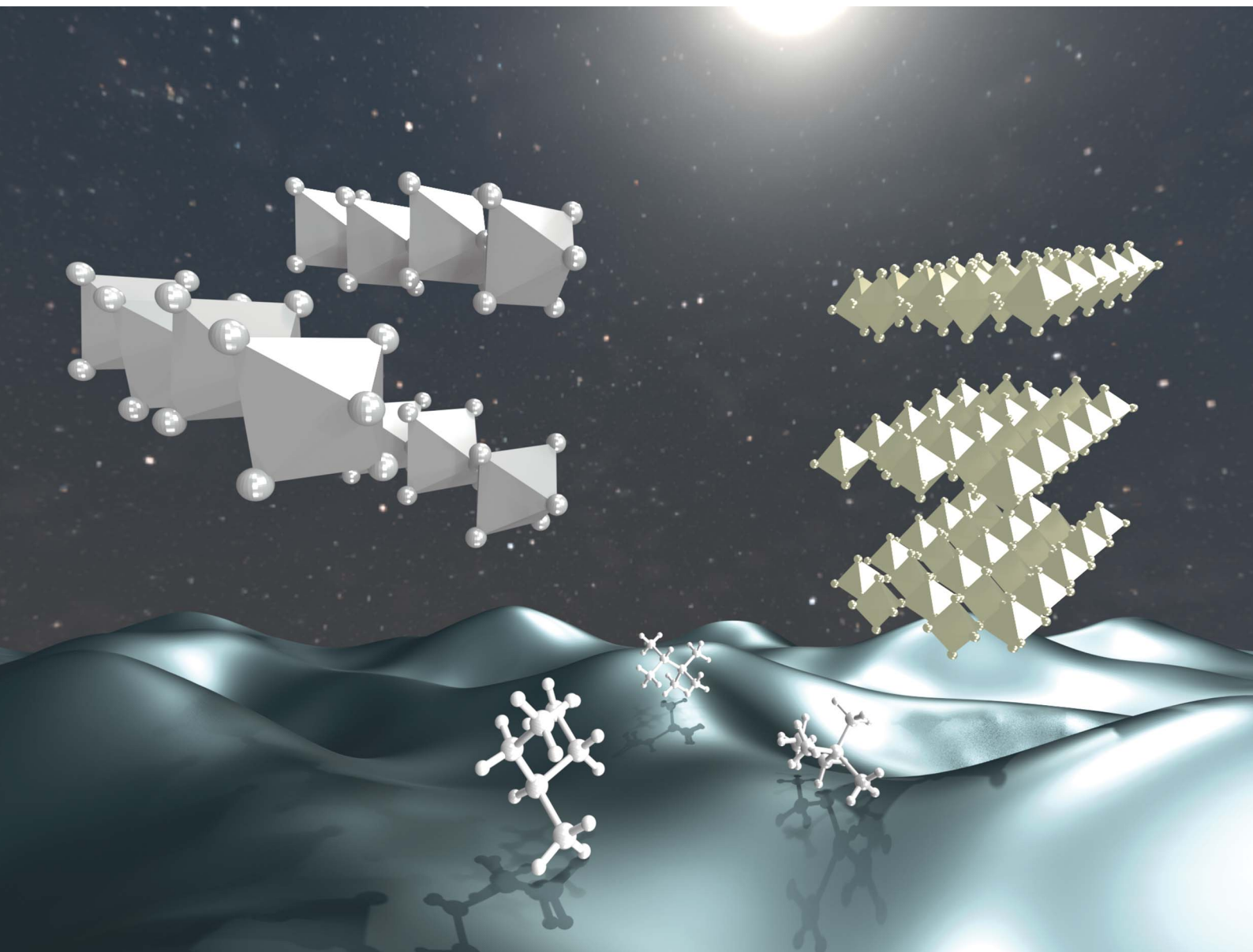


Journal of Materials Chemistry A

Materials for energy and sustainability

rsc.li/materials-a



ISSN 2050-7488

PAPER

L. Catherine Brinson *et al.*
Uncertainty-aware dimensionality prediction of
low-dimensional hybrid metal halides by integrating
Bayesian modeling and experiments

Cite this: *J. Mater. Chem. A*, 2026, **14**, 18589

Uncertainty-aware dimensionality prediction of low-dimensional hybrid metal halides by integrating Bayesian modeling and experiments

Migon Choi,^a Dongkyu Derek Cho,^b Richard Sheridan,^a David B. Mitzi^{ac} and L. Catherine Brinson^{id}*^a

Data-driven materials informatics is revolutionizing materials design by uncovering complex structure–property relationships beyond traditional trial-and-error methods. In perovskites and more generally hybrid metal halides (HMHs), comprising metal halide anions and organic spacer cations, variations in the spacer cations can alter the inorganic framework dimensionality, which has direct consequences for optical and electronic properties. In this paper, we explore the factors impacting HMH dimensionality, with a focused experimental study and a broad materials informatics approach. Experimentally, we employed three structurally similar branched alkyl cations. Despite their close similarity, they produced distinct lead iodide hybrid frameworks: one forming a 2D layered structure and two forming 1D chain phases. These results confirm that molecular differences can dictate dimensionality. Expanding from these observations, we curated a dataset of 113 HMHs and applied Bayesian additive regression trees to predict dimensionality from molecular descriptors. Here, we show that Bayesian additive regression trees achieved a strong predictive power (posterior mean area under the curve of around 0.8) while quantifying uncertainty. The results highlight organic cation aspect ratio, polar surface area, and the number of branched points as dominant features for dimensionality prediction. An active learning strategy further enhanced model net improvement by ~20%, increasing the efficiency of identifying promising candidates compared to random sampling. Together, this study provides both experimental evidence and machine learning rules that clarify how spacer cation structure governs HMH dimensionality, offering a data-driven path to rational design of low-dimensional hybrid semiconductors. By integrating experimental observations with data-driven modeling, this study highlights the potential of materials informatics to guide predictive design across structurally diverse material systems and motivates broader curation of well annotated materials datasets.

Received 5th December 2025
Accepted 1st April 2026

DOI: 10.1039/d5ta09980c

rsc.li/materials-a

1. Introduction

Advances in materials informatics are transforming the way materials are designed and optimized, enabling the discovery of structure–property relationships beyond conventional trial-and-error approaches.^{1,2} These data-driven methods have shown great promise for tackling complex material systems where chemical variations can lead to drastic changes in structure and performance, such as hybrid perovskites, where molecular variations can lead to dramatic shifts in structure. For instance, a slight change in the organic spacer cation can alter crystal dimensionality (*i.e.*, referring to connectivity of the inorganic

framework), switching the material's optoelectronic behavior and long-term stability.^{3–7}

Hybrid perovskites represent a class of materials, generally comprising an extended framework of corner-sharing metal halide octahedra alternating with regions of organic cations.⁸ These semiconductors have shown outstanding potential in optoelectronic devices, due to low processing cost, tunable band gap, and high efficiency.^{9–12} The structural diversity is remarkable, and their performance depends on the relationship between structure, processing, properties, and performance.^{13,14} The dimensionality of these frameworks – whether the crystal forms 0D, 1D, 2D, or 3D – impacts optoelectronic properties, such as light absorption and charge transport.^{15–17} Therefore, controlling dimensionality is critical for efficient and stable devices based on these semiconductors. Given that our study includes octahedra sharing paradigms beyond conventional corner-sharing perovskites (*e.g.*, corner-, edge-, or face-sharing), we collectively refer to these materials as hybrid metal halides

^aDepartment of Mechanical Engineering and Materials Science, Duke University, Durham, North Carolina, 27708, USA. E-mail: cate.brinson@duke.edu^bDepartment of Statistical Science, Duke University, Durham, North Carolina, 27708, USA^cDepartment of Chemistry, Duke University, Durham, North Carolina 27708, USA

(HMHs), a broader class of which hybrid organic–inorganic perovskites represent a special subset.

In low-dimensional HMHs, the organic spacer cation plays a key role in determining the resulting structure. Recent studies have shown that both structural and electronic features of the spacer – such as aromaticity, steric hindrance, and dielectric constant – can significantly influence the HMH's structure, properties, and performance.^{18–20} Despite these insights, the selection of spacer cations has largely relied on researchers' intuition, and a systematic, data-driven understanding of how molecular features govern HMH dimensionality remains limited. Recent studies demonstrate that machine learning (ML) can extract meaningful design rules for low-dimensional HMHs. Lyu *et al.* showed that steric and hydrogen-bonding descriptors can distinguish whether a spacer forms 2D frameworks.²¹ Mai *et al.* applied descriptor-based regression modeling at the device level, using feature-importance analysis to identify molecular properties most correlated with power conversion efficiency.²² Other works, such as database-driven band-gap modeling²³ and ligand screening for stability,²⁴ further highlight the potential of ML in this space. While these studies provide valuable advances, a systemic understanding of how spacer descriptors relate to dimensionality within experimentally accessible, data-limited regimes remains limited. Moreover, most prior ML approaches rely on point-estimate models without addressing predictive uncertainty, which is an important consideration for reliable predictions in the small, heterogeneous datasets common in experimental materials research.

Within this framework, we apply machine learning to investigate how variations in spacer cation structure influence HMH dimensionality. We scope our work to a specific experimental regime defined by Pb–I based frameworks and comparable synthesis protocols, and how molecular-level descriptors of spacer cations can support probabilistic predictions of dimensionality within this constrained space. We utilized Bayesian Additive Regression Trees (BART) as our primary predictive model, with a Random Forest classifier (RF classifier) serving as the baseline. Unlike conventional classifiers, BART provides not only predictions but also posterior predictive uncertainty.²⁵ In data-limited and heterogeneous materials systems, quantifying uncertainty is crucial for identifying overconfident extrapolation and assessing the reliability of model predictions.^{26–28}

To ground our machine learning analysis, we start with experimental observations showing that variations in branched alkyl spacer cations lead to distinct HMH dimensionalities. To capture these trends systemically, we begin with three experimentally realized systems derived from organic spacers based on branched alkyl amines: 3,3-dimethylbutylamine (3,3-DMBA), 2,3-dimethylbutan-2-amine (2,3-DMB2A), and *N*-methylbutan-2-amine (NMB2A), each combined with PbI₂ under identical conditions. Variations in the spacer cations drive different outcomes, yielding a 2D layered phase ((3,3-DMBA·H)₂PbI₄) versus 1D chain motifs ((2,3-DMB2A·H)PbI₃ and (NMB2A·H)PbI₃). Motivated by these experimental insights, we subsequently broaden our machine learning analysis to explore

a wider chemical space by combining data curated from the literature with an existing data resource. Using the classification models, we predict the dimensionality of HMH structures and systematically investigate the most influential molecular features that govern this outcome. Finally, through a simulated active learning cycle with BART, we highlight how its uncertainty-aware framework can both enhance predictive performance and provide interpretable cluster-level insights, pointing to its potential for future experimental application.

This work presents a framework for the data-driven design of low-dimensional HMH structures, including hybrid perovskites, offering new insight into the relationship between molecular structure and dimensionality. Our goal is not a universally generalizable model, but the development of an uncertainty-aware, data-driven framework that can inform experimental decision-making under realistic data limitations. While demonstrated here for low-dimensional HMHs, the conceptual framework – particularly the emphasis on uncertainty-aware learning in data-scarce regimes – may be informative for other hybrid materials systems, such as Covalent Organic Frameworks (CoFs),²⁹ and van der Waals layered materials,³⁰ where structural diversity complicates rational design. In particular, the uncertainty-aware nature of BART makes it powerful in data-scarce regimes, where experimental throughput is limited, and predictive reliability is crucial.^{31,32}

2. Methods

2.1. Crystal growth and characterization

Single crystals were obtained by slow evaporation of PbI₂ with the corresponding organic amines in HI/methanol solutions. Stoichiometries of 1 : 1, 2 : 1, and 4 : 1 spacer-to-lead ratios were explored. Exact reagent quantities and conditions are summarized in SI (1. Single crystal growth). Structural analysis was conducted using PXRD and SCXRD, while optical properties were probed by UV-vis and PL spectroscopy. Thermal stability was assessed by TGA. Full instrument specifications and measurement parameters are provided in SI (2. Characterization).

2.2. Data handling

A dataset of 113 HMHs was compiled from the Hybrid3 database (available at <https://hybrid3.duke.edu/>), the literature, and our experimental results. Chemical names and dimensionality labels were obtained directly from these sources, while molecular descriptors were computed separately as described in Section 2.3. Descriptors in methods section. Hybrid3 database provides 11 1D structures, which was supplemented with 26 additional 1D structures, including 2 generated in our experiments and 24 collected from the literature, resulting in a total of 37 1D entries. We also included 76 2D structures, of which 75 came from the Hybrid3 database and 1 from our experiments. To ensure consistency, we only retained lead iodide-based single-crystal samples with 1D or 2D structures, and organic cations that could be converted to SMILES strings (Table S3). The final dataset comprised 113 entries (76 2D and



37 1D). More detailed filtering criteria are described in SI (3. Data handling). The data were split into training and test sets (Train: 84, Test: 29) for Sections 3.2.1 (Model performance and uncertainty quantification) and 3.2.2 (Feature importance); into training, test, and experimental sets (Train: 82, Test: 28, Experimental: 3) for Section 3.2.3 (Demonstration on synthesized structures); and into training, test, and pool sets (Train: 69, Test: 29, Pool: 15) for Section 3.2.4 (Active learning). For active learning, 6 samples with the highest information gain were selected from the pool set and added to the training set. Before machine learning, data were label encoded for categorical descriptors and min-max scaled. Pairwise Controlled Manifold Approximation Project (PaCMAP³³) analysis is employed to visualize the high-dimensional data (see Section 4. PaCMAP in SI). The PaCMAP embedding does not preserve interpretable coordinates; rather, it provides a visualization of the sample distribution in reduced space. The relative proximity between points reflects similarity based on the input descriptors. The categorical descriptor (nitrogen atom position) is omitted for PaCMAP analysis.

Because the present dataset is restricted to Pb–I frameworks and limited in size, the analysis focuses on spacer-driven dimensional trends; incorporation of inorganic geometric descriptors and connectivity subclasses represents an important direction for future expansion as larger standardized datasets become available.

2.3. Descriptors

To capture the key molecular factors governing HMH dimensionality, we gathered ten chemically interpretable descriptors that reflect steric, electronic, and geometric characteristics of the spacer cations. These include the number of carbon and nitrogen atoms, rotatable bonds, aromatic rings, hydrophobicity ($\log P$), polar surface area (PSA), aspect ratio, van der Waals volume, nitrogen atom position, and number of branched point (see Section 5. Descriptors in SI, Table S3). The selected descriptors were chosen to represent parameters known to influence intermolecular interactions, packing motifs, and hydrogen-bonding environments in HMHs.^{34,35} Specifically, steric and geometric descriptors (*e.g.*, aspect ratio, number of branched points, van der Waals volume) capture the spatial constraints affecting layer spacing and packing density, while electronic and polarity-related descriptors (*e.g.*, $\log P$, PSA) account for variations in hydrogen bonding and ionic interactions that modulate the stability and dimensionality of the resulting structures.^{36–38} While synthesis conditions can impact crystal formation, because of inconsistent reporting of processing steps in the literature and lack of clear annotated metadata on synthesis in the available database, no descriptors related to synthesis conditions are utilized. As discussed later, this represents a significant opportunity for future research.

2.4. Machine learning

Machine learning methods, including tree-based regression and deep learning models, have demonstrated strong empirical success when trained on large-scale datasets.^{39–41} With sufficient

data, these models benefit from asymptotic convergence of parameters, yielding stable estimators without explicitly quantifying uncertainty. However, in materials science applications, the conditions for such asymptotic guarantees are rarely met, as experimental datasets are often small and heterogeneous. Under these circumstances, point estimates of predictive performance can be misleading, and it becomes essential to explicitly capture uncertainty. Quantifying uncertainty is therefore essential for identifying when the model is extrapolating and for guiding decisions based on the reliability of each prediction.^{26–28} Bayesian Additive Regression Trees (BART)²⁵ offers a potential solution for this setting. BART provides a posterior predictive distribution, enabling uncertainty quantification without relying on restrictive parametric assumptions. While traditional ensembles such as Random Forest (RF)⁴² can achieve comparable accuracy, they deliver only point estimates by default and lack principled measures of uncertainty.

BART constructs its final prediction as an ensemble of shallow decision trees, using a regularization prior which prevents overfitting. During training, it uses Markov chain Monte Carlo to sample from the posterior distribution over tree structures and leaf parameters. Each posterior draw corresponds to one model instance, which in turn produces a prediction; aggregating these draws yields the predictive distribution. From this distribution, we can quantify uncertainty, for example, by computing credible intervals. We demonstrate how BART captures per-sample predictive uncertainty through posterior probability intervals and summarizes model-level performance using a posterior distribution of the area under the receiver operating characteristic curve (AUC).⁴³ AUC is a standard metric used to evaluate how well a classification model distinguishes between two classes. An AUC of 0.5 corresponds to random guessing, whereas an AUC of 1.0 indicates perfect separation. In a Bayesian model, each prediction is expressed as a posterior probability, the estimated likelihood that a given sample belongs to a specific class. Instead of providing a single fixed prediction like RF, the model produces a distribution of possible probabilities, from which credible intervals can be derived. We further show how BART can be applied to active learning. Additional details are provided in SI (see Sections 6. Random forest classifier (RF), 7. Bayesian additive regression trees (BART), and 8. Model interpretation and active learning evaluation).

3. Results and discussion

In the following section, we present the key findings of our study. We first grew single crystals of HMHs based on three chemically distinct yet structurally related branched alkyl ammonium spacers. Structural and optical characterizations of these crystals confirmed the expectation that variations in spacer molecular structure can lead to distinct dimensionalities. Motivated by these observations, we expanded our scope using machine learning. After collecting and curating a dataset (details of curation and data splitting are provided in the Methods section, 2.2. Data handling), we applied BART²⁵ to investigate whether variations in spacer cations could predict



1D versus 2D dimensionalities with the training from this larger dataset. We further analyzed the relative importance of molecular descriptors to identify features that most strongly influence dimensionality. Building on these findings, we implemented an active learning framework to demonstrate its potential utility for guiding future spacer cation selection in experimental studies. Finally, we conducted PaCMAP analysis to explore regions of molecular space where experimental exploration would most improve predictive performance.

3.1. Dimensional control *via* spacer cation structure

As an initial demonstration, we investigated three spacer amines: 3,3-dimethylbutylamine, 2,3-dimethylbutan-2-amine, and *N*-methylbutan-2-amine (Fig. 1). We combined these spacer amines with PbI_2 under identical conditions, resulting in their protonation and insertion as spacer cations in the final HMH structures. While all three amines share the similarities of being aliphatic and branched, the HMH structure outcomes diverged: 3,3-dimethylbutylamine yielded a 2D layered structure based on corner-shared octahedra ($(3,3\text{-DMBA}\cdot\text{H})_2\text{PbI}_4$), while the other two produced 1D chain structures with face-sharing connectivity ($(2,3\text{-DMB2A}\cdot\text{H})\text{PbI}_3$ and $(\text{NMB2A}\cdot\text{H})\text{PbI}_3$), as confirmed by X-ray diffraction (Fig. 2, S1–S3 and Tables S1, S2).

Optical spectroscopy further reflected this dimensional contrast (see 2.2. Optical properties in SI). The 2D phase exhibited excitonic absorption/emission near 483/491 nm, consistent with typical 2D HMHs.^{44,45} In contrast, the 1D phases showed blue-shifted absorption/emission ($\approx 385/458$ nm and $\approx 381/414$ nm), in line with trends in reduced-dimensional systems^{46–48} (Fig. S4–S6). Our experiments confirm that systematic variations in spacer molecular structure are sufficient to shift crystal dimensionality and tune optical response. Beyond these primary outcomes, stoichiometry variation may also lead to additional motifs, including corner-sharing and trimer-type 1D phases (Fig. S7–S10; 2.3. Single crystal X-ray diffraction (SCXRD) for additional crystallographic refinements and characterization in SI).

To contextualize the synthesized samples within the overall chemical space, we visualized their locations relative to our entire curated dataset. All data are presented in the PaCMAP visualization (Fig. 3) showing a clear clustering of the complete 113 sample dataset into 3 clusters, where the positions of the synthesized samples are noted by red circles. Fig. S11 shows the molecular feature profiles of the three clusters. Group 1, which includes the three synthesized samples, corresponds to more alkyl-like spacer structures with lower van der Waals volume, fewer aromatic rings, and reduced polar surface area. Group 0 represents molecules with moderate polar surface area,

whereas group 2 consists of molecules with higher polar surface areas, multiple nitrogen atoms, and greater flexibility. Although these clusters differ in molecular descriptors and structural descriptors, the distribution of 1D and 2D HMHs is relatively balanced across groups, indicating that the grouping discovered by PaCMAP primarily reflects molecular structural similarity.

Yet, despite the apparent closeness for the 3 synthesized samples, their experimental outcomes diverged. The sensitivity revealed by this discrepancy motivated us to develop a machine learning framework aimed at predicting the dimensionality of HMH phases. It is acknowledged that identical spacer cations can result in different structural configurations (*e.g.*, dimensionality and/or connectivity) depending on the synthesis conditions (*e.g.*, precursor ratio) (Fig. S7 and S8; 2.3. Single crystal X-ray diffraction (SCXRD) in SI for additional crystallographic refinements and characterization). Indeed, in the chemical space examined here, spacer-to-lead stoichiometry represents a experimentally demonstrated control parameter for dimensionality and connectivity in our 3 synthesized samples, as evidenced by the ratio-dependent motif changes observed in Fig. S7–S10. However, because synthesis parameters such as precursor stoichiometry, solvent environment, and temperature are not systematically available across published reports or as tagged metadata in the Hybrid3 database, in the subsequent machine learning analysis synthesis parameters cannot be encoded as features, and we thus assume that each spacer cation corresponds to a single dimensionality. Accordingly, the model should be interpreted as capturing spacer-intrinsic structural tendencies within typical synthetic contexts, rather than predicting a complete synthesis-dependent phase diagram. This assumption of 1:1 cation-dimensionality correspondence may restrict our predictive performance and motivates future efforts toward active data sharing within the community to collect and clearly annotate more comprehensive synthesis and processing information.

3.2. Machine learning

In this section, we extend our experimental findings by applying Bayesian additive regression trees. We evaluate model performance and uncertainty quantification (3.2.1. Model performance and uncertainty quantification), analyze feature importance (3.2.2. Feature importance) and apply BART to the synthesized structures (3.2.3. Demonstration on synthesized structures). We further demonstrate how BART can be used to perform active learning (3.2.4. Active learning).

3.2.1. Model performance and uncertainty quantification.

We first established a Random Forest (RF)⁴² baseline that achieved an AUC of 0.82 (see Data availability for details). While this represents a reasonably strong predictive performance, understanding the model's predictive uncertainty is essential, particularly in studies like this where heterogeneous materials data can introduce variability. To quantify predictive uncertainty and overall model performance, we employed a Bayesian additive regression tree (BART)²⁵ model. Unlike conventional ensemble methods such as RF, BART provides full posterior

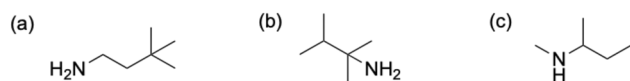


Fig. 1 Choice of amines, where (a) 3,3-dimethylbutylamine (3,3-DMBA), (b) 2,3-dimethylbutan-2-amine (2,3-DMB2A), and (c) *N*-methylbutan-2-amine (NMB2A).



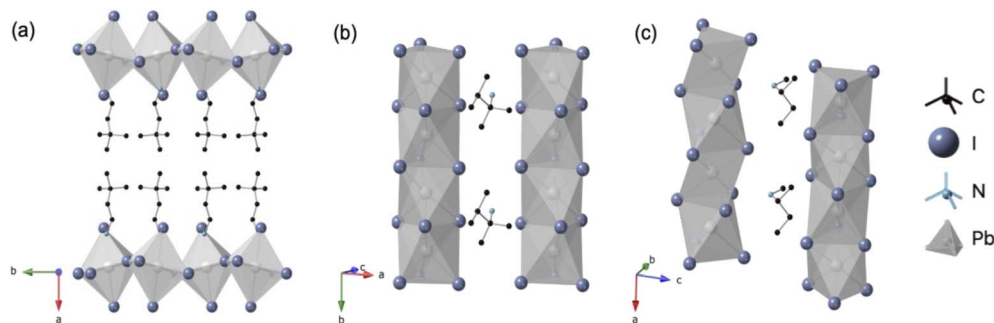


Fig. 2 Schematic single-crystal structures of (a) $(3,3\text{-DMBA}\cdot\text{H})_2\text{PbI}_4$, (b) $(2,3\text{-DMB2A}\cdot\text{H})\text{PbI}_3$, and (c) $(\text{NMB2A}\cdot\text{H})\text{PbI}_3$.

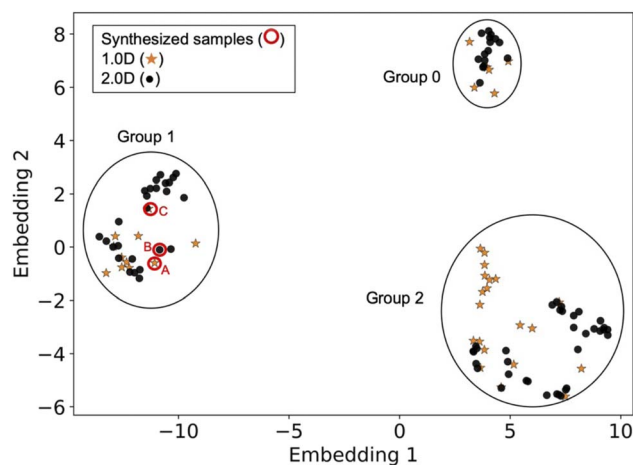


Fig. 3 Two-dimensional embedding of the spacer cation descriptors of our curated dataset (gold stars: 1D, black dots: 2D) generated using the PaCMAP algorithm. Cations with similar descriptors will appear close to each other in this projection. The three synthesized samples are highlighted by red circles, where A = 2,3-DMB2A, B = 3,3-DMBA, C = NMB2A. Groups show a good mixture of both 1D and 2D data.

distributions over model parameters, allowing uncertainty estimation for both individual predictions and global performance metrics (Fig. 4 and S12–S14). Fig. 4(a) illustrates composition-level predictive uncertainty from BART: for each test sample, the model outputs a posterior mean probability along with a 94% highest density interval (HDI); that is, the model predicts a given new sample is 1D or 2D with a specific probability (the black dot in Fig. 4(a)) and indicate of its confidence in this prediction (the orange bar in Fig. 4(a)). Samples with narrow HDIs (orange bars) indicate confident predictions supported by consistent training patterns, whereas wide HDIs reflect regions of higher uncertainty, likely due to limited or conflicting data.

To summarize classification performance across all thresholds, we further examined the posterior distribution of the area under the receiver operating characteristic curve (AUC),⁴³ shown in Fig. 4(b). Each value in this distribution corresponds to the AUC computed from one posterior draw of the trained model, reflecting uncertainty in the model's discriminative ability. The

posterior mean AUC on the test set was 0.837, with a 95% credible interval of 0.750–0.909.

To qualitatively assess model behavior on the test set, we projected all test samples into a 2D PaCMAP embedding similar to Fig. 3, shown in Fig. S15, coloring points by their ground-truth dimensionality and marking prediction correctness. Note that in this analysis, the newly synthesized 3 experimental samples are simply part of the entire data pool and are thus selected randomly into test or train sets. Although 1D and 2D samples are not completely separated, correct predictions dominate within the major clusters (5/7 for 1D and 20/22 for 2D). Additional diagnostic results suggest satisfactory convergence and mixing across all chains, with effective sample sizes (ESS) generally above 4000 and R -hat values close to 1.00 (Fig. S12 and S13).

3.2.2. Feature importance. To understand which molecular features most strongly influence the dimensionality outcome, we examined feature importance in the trained models. Feature importance analysis quantifies how much each input variable contributes to a model's predictions, providing interpretability and physical insight into otherwise complex models. In chemical discovery, such analysis can reveal structure–property relationships that guide rational molecular design. In this study, permutation importance was used as the primary measure of feature relevance for both the BART and RF models. This approach evaluates the decrease in model performance when the values of a given feature are randomly shuffled, thereby quantifying how strongly the model depends on that feature for accurate prediction. To complement this analysis, the BART model's built-in feature importance²⁵ and the RF model's SHAP (Shapley Additive exPlanations)⁴⁹ values were also examined to assess consistency across interpretability methods (Fig. 5 and S16–S18). Both the BART and the RF classifier model consistently identified aspect ratio, polar surface area (PSA), and the number of branched points as the most influential descriptors for predicting HMH dimensionality (Fig. 5, S16 and S17). To further interpret how these features contribute to the model's decision-making, we analyzed the RF model with SHAP (Fig. S18). SHAP analysis indicates that increasing PSA and aspect ratio, while decreasing the number of branching points, tends to favor the formation of 2D structures. These descriptors capture structural and electronic factors that influence spacer



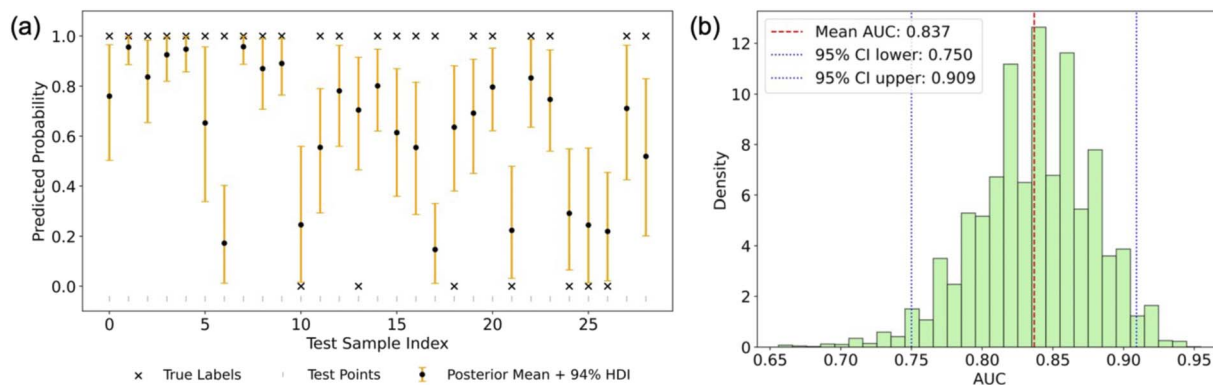


Fig. 4 Posterior predictive performance and uncertainty of the BART model on the test set. (a) Posterior predictive probabilities for test samples (1D vs. 2D). Black dots represent posterior mean predictions from the BART model, while orange bars indicate 94% highest density intervals (HDIs) capturing predictive uncertainty. True labels (x) are binary, where 0 corresponds to 1D samples and 1 corresponds to 2D samples. Although the true labels are discrete (0 or 1), the model outputs continuous probabilities between 0 and 1, reflecting uncertainty in the predicted class. (b) Histogram of posterior AUC values computed from 40 000 posterior draws of the model. The y-axis shows the probability density of AUC values obtained from posterior samples. The red dashed line indicates the mean AUC of the BART model (0.837), and blue dotted lines denote the 95% credible interval (0.750–0.909).

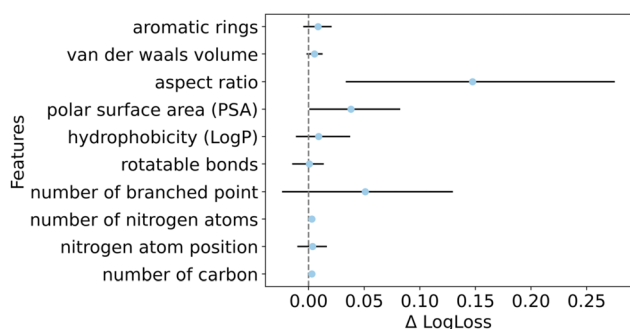


Fig. 5 Permutation importance for BART based on posterior means with 95% credible intervals.

cation-inorganic framework interactions and packing geometry in low-dimensional HMHs.

The data-driven approach integrates diverse molecular descriptors into a unified quantitative framework, moving beyond intuition-based assessments of individual features, and providing a quantitative context that connects with prior studies emphasizing specific molecular parameters. As PSA increases, the probability of forming a 2D phase rises; this is consistent with reports that N–H...I hydrogen bonding and electrostatic interactions between ammonium spacers and halides strengthen interfacial cohesion and interlayer networks in 2D Ruddlesden–Popper phase HMHs.^{37,45,50} A larger aspect ratio correlates with a higher likelihood of 2D formation: slender, more anisotropic spacer cations promote parallel alignment and dense in-plane packing of the organic bilayers, stabilizing extended 2D slabs; in contrast, bulkier/shorter shapes introduce corrugation and packing frustration that bias chain-like (1D) motifs. This interpretation aligns with studies showing that spacer packing arrangements and orientational order control film structure and energetics, and that linear, longer-chain spacers enhance molecular organization.^{51,52} In layered

HMHs, branching near the ammonium headgroup increases steric demand that can hinder planar tiling and sheet continuity, increasing interlayer spacing and steering Dion–Jacobson and Ruddlesden–Popper structural evolution; in certain chemistries, branched headgroups can also stabilize 1D chains (*e.g.*, isopropylammonium lead iodide).^{53,54} Thus, while the statistical analysis from these models cannot provide direct mechanistic proof, their ability to capture nonlinear feature interactions and patterns in the data provide researchers with strong evidence to connect to physical mechanisms.

3.2.3. Demonstration on synthesized structures. To probe the practical relevance of the BART model beyond curated datasets, we tested it on the three structures synthesized in our laboratory. In this analysis, these samples, (3,3-DMBA·H)₂PbI₄, (2D), (2,3-DMB2A·H)PbI₃ (1D), and (NMB2A·H)PbI₃ (1D), were excluded from the training/testing pipeline and only introduced afterward as out-of-sample cases (see Section 2.2).

With this data split analysis, the model achieved a posterior mean AUC on the test set of 0.72. Out of the three predictions, two were correct: (3,3-DMBA·H)₂PbI₄, (2D) and (2,3-DMB2A·H)PbI₃ (1D) (Fig. 6). The misclassified case, (NMB2A·H)PbI₃ (1D), is noteworthy as the trained model provides an incorrect classification with relatively high confidence. The misclassification of (NMB2A·H)PbI₃ highlights an important limitation of relying primarily on steric and geometric descriptors. Although NMB2A exhibits a relatively high aspect ratio and low branching – features that statistically correlate with 2D formation in our dataset – it experimentally stabilizes a 1D face-sharing structure. Notably, NMB2A is the only secondary amine among the three spacers, which may influence hydrogen-bonding geometry and packing interactions. This suggests that steric descriptors alone may not fully capture the balance between organic packing constraints and inorganic framework energetics that governs connectivity selection. Face-sharing motifs may be influenced not only by spacer geometry but also by hydrogen-bonding geometry, lattice strain accommodation,



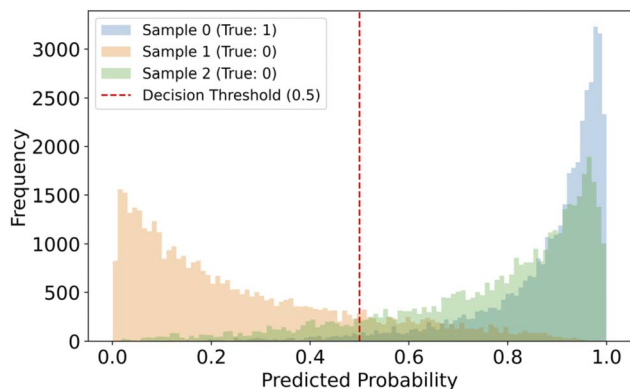


Fig. 6 Posterior probability distributions for three newly synthesized spacer cations, which were excluded from model training and evaluated as out-of-sample cases. Samples 0, 1, and 2 correspond to (3,3-DMBA·H)₂PbI₄, (2,3-DMB2A·H)PbI₃, and (NMB2A·H)PbI₃, respectively. In the legend, “True: 1” denotes samples with a true (experimentally observed) 2D structure, and “True: 0” denotes samples with a true 1D structure. The decision threshold (0.5) marks the probability cutoff used for classification: predicted probabilities above 0.5 correspond to 2D, and those below 0.5 correspond to 1D.

and possible solvent-mediated stabilization. The NMB2A case therefore underscores that dimensionality emerges from a coupled organic–inorganic system, and that spacer-only descriptors capture dominant statistical trends but cannot universally resolve all structural outcomes. Future extensions incorporating additional structural and processing descriptors may help clarify such boundary cases.

3.2.4. Active learning. Active learning is an iterative machine learning approach that selects new data points expected to improve the model, through criteria such as uncertainty reduction or performance enhancement.⁵⁵ In this study, rather than training on a fixed dataset, the model identifies candidates expected to provide the greatest information gain (IG), quantified using the Bayesian Active Learning by Disagreement criterion.⁵⁶ These candidates, those for which the model’s posterior predictions are most uncertain across samples, are then prioritized for experimental validation. We conducted an active learning experiment using BART by calculating the information gain (IG)⁵⁶ for all 15 candidate samples in the pool set (recall for this analysis we split the data as Train: 69, Test: 29, Pool: 15; see Data handling Section 2.2) and selecting the 6 with the highest IG for model retraining (Fig. 7 and S19). The improvement or degradation of model performance after active learning was determined using mutual information (MI) and log loss, which respectively measure the dependency between variables and the accuracy of probabilistic predictions. After retraining, among the 29 test samples, 14 samples showed improved performance while 3 samples worsened, which achieved net improvement of 37%, defined as (improved – worsened)/total × 100. This outcome is notable because, in comparison, running active learning with randomly selected samples yielded an average net improvement of 15 ± 26% (8 runs). By leveraging IG for active learning, the rate of worsened

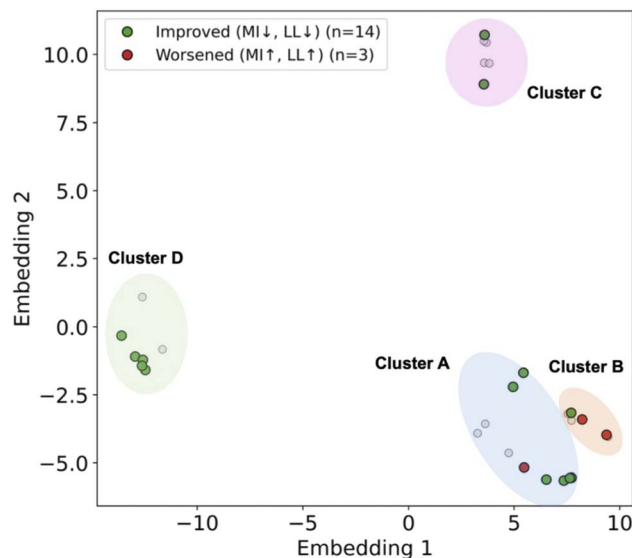


Fig. 7 Two-dimensional PaCMAP embedding plot of samples, where the green dots represent samples that improved after model update (MI ↓, LL ↓, $n = 14$), the red dots represent samples that worsened (MI ↑, LL ↑, $n = 3$), and the uncolored dots indicate samples with no change. MI = mutual information; LL = log loss. Cluster B contains a higher fraction of red samples, corresponding to highly branched and polar spacers that showed limited improvement during active learning.

samples was reduced from 20 ± 13% to 10%, representing an approximate 10% relative improvement in model stability.

These results illustrate the potential practical advantage of uncertainty-driven active learning within this dataset. Reductions in mutual information and log loss correspond to improved confidence and calibration in probabilistic predictions, which in turn enhance the reliability of selecting candidate spacers for experimental validation. In this study, information-gain-based selection identified successful candidates at a higher rate than random sampling across multiple independent trials. While demonstrated within a constrained candidate pool, this result suggests that uncertainty-aware acquisition can improve experimental efficiency in small-data regimes.

To better understand the structural space, we identified representative clusters in Fig. 7 and quantified the net improvement within each cluster (Fig. 8). The cluster feature interpretation is derived from *post-hoc* descriptor analysis. This analysis was based on the three most influential descriptors based on feature importance (Fig. 5): aspect ratio, polar surface area (PSA), and the number of branch points (branching). Radar plots illustrate the relative magnitude of key descriptors within each cluster. The polygon area and shape highlight which features (*e.g.*, aspect ratio, PSA, and branching) are more dominant in each cluster. The results revealed that clusters A, C, and D exhibited positive net improvements, corresponding to high-aspect ratio molecules (cluster A), structurally balanced molecules (cluster C), and compact, simple molecules (cluster D). In contrast, cluster B, characterized by a high degree of branching and large PSA, showed a negative net improvement.



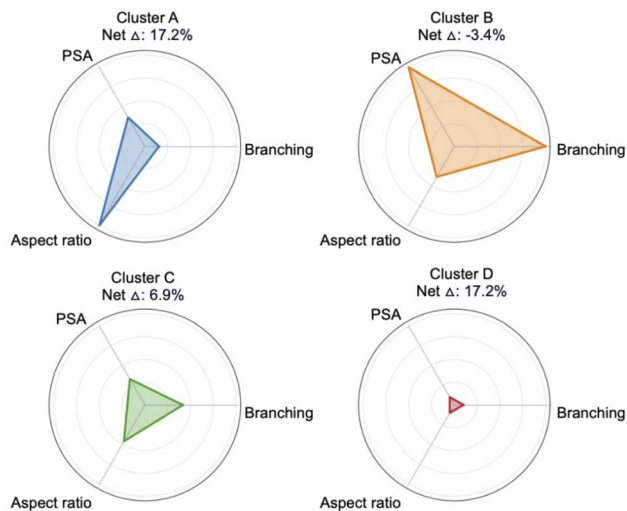


Fig. 8 Cluster-wise radar plots showing structural profiles of spacer cations based on three key descriptors: number of branched points (branching), polar surface area (PSA), and aspect ratio. Descriptor values are presented on a normalized (relative) scale, enabling comparison of their relative magnitudes across clusters.

This indicates that targeted experimental sampling within this region of the feature space could enhance the model's representation and predictive performance in subsequent iterations. Within the current dataset, compact, simple, and high-aspect ratio structures appear more favorable for optimization. However, this trend should be interpreted with caution, as highly polar or branched spacers may interact nonlinearly with other descriptors. With more data or expanded features, these spacers could exhibit different behaviors, emphasizing the need to preserve chemical diversity in future active learning cycles. At present, it remains unclear whether such regions reflect intrinsic phase competition or sparse sampling in descriptor space, further underscoring the importance of expanded and condition-aware datasets.

4. Conclusions

In this study, we investigated the dimensionality prediction of low-dimensional Hybrid Metal Halides (HMHs) by combining experimental synthesis and data-driven modeling. Experimentally, we synthesized new low-dimensional HMH crystals based on branched alkyl-based ammonium cations and confirmed that variations in spacer cations influence both the structural dimensionality and the optical properties within this family. Motivated by these observations, we extended the study to a data-centric approach by integrating data from the Hybrid3 repository, literature sources, and newly synthesized structures into a unified dataset. Molecular descriptors were computed using RDKit software and visualized with PaCMAP embedding, which suggested grouping patterns related to spacer-cation properties.

Based on this dataset, we developed a machine-learning framework to classify HMH dimensionality. The Bayesian Additive Regression Tree (BART) model achieved a posterior

mean AUC of 0.83, which is comparable to that of the random forest baseline. While both models provide similar predictive performance, BART additionally offers posterior probability distributions that quantify prediction confidence. This uncertainty estimation is particularly valuable for small and heterogeneous datasets that are common in experimental materials research. Feature-importance analysis identified three key molecular factors that govern dimensionality: aspect ratio, polar surface area, and the number of branched points. Incorporating an active learning strategy further improved net improvement by approximately 20 percent.

Overall, this uncertainty-aware framework establishes a predictive approach that links molecular structure to emergent dimensionality. The methodology can be extended to larger and more diverse datasets and ultimately provides a foundation for data-driven design of next-generation hybrid materials. The work also motivates a need for more curated experimental data sets with more complete metadata annotation, especially capturing the synthesis and processing features. Given the existence of text based information in the literature, coupled with complexities of defining a standard for data reporting in publications, future work integrating natural language processing-based extraction of synthesis conditions and broader families of spacer cation-inorganic stoichiometries is a promising pathway. Such work would allow inclusion of a richer set of descriptors for future data driven exploration and expand the accessible design space and enhance structural predictability.

Author contributions

M. C.: conceptualization; methodology; software; data curation; formal analysis; investigation; visualization; writing – original draft; writing – review & editing. D. D. C.: methodology; validation; writing – review & editing. R. S.: validation; writing – review & editing. D. B. M.: conceptualization (experimental); supervision (experimental); writing – review & editing. L. C. B.: conceptualization; methodology; supervision; writing – review & editing.

Conflicts of interest

There are no conflicts of interest to declare.

Data availability

The datasets and machine learning codes supporting this study are available on GitHub at (<https://github.com/migonchoi/Perovskite-Dimensionality-Prediction>) and Duke Research Data Repository (RDR) (<https://doi.org/10.7924/r4n87ht86>).

CCDC 2490415 ((3,3-DMBA·H)₂PbI₄), 2490430 ((2,3-DMB2A·H)PbI₃) and 2490431 ((NMB2A·H)PbI₃) contain the supplementary crystallographic data for this paper.^{57a-c}

Supplementary information (SI): detailed experimental procedures, additional characterization data (XRD, UV-Vis, PL, SCXRD, TGA, and FTIR), crystallographic tables, data processing methods, molecular descriptor definitions, and full



descriptions of the machine learning models along with model interpretation and active learning analyses. See DOI: <https://doi.org/10.1039/d5ta09980c>.

Acknowledgements

M. C. and D. B. M. acknowledge support from National Science Foundation under award number DMR-2323547. R. S. and L. C. B. acknowledge support from National Science Foundation under award number DGE-2022040. We thank Dr Yi Xie for guidance in selecting the three spacer cations and for early support with crystal growth, SCXRD, and structural refinement. We also thank Dr Rayan Chakraborty for assistance with crystal structure refinement.

References

- D. Sivan, K. Satheesh Kumar, A. Abdullah, V. Raj, I. I. Misnon, S. Ramakrishna and R. Jose, *J. Mater. Sci.*, 2024, **59**, 2602–2643.
- R. Ramprasad, R. Batra, G. Pilania, A. Mannodi-Kanakkithodi and C. Kim, *npj Comput. Mater.*, 2017, **3**, 54.
- X. Liu, H. Yan, Z. Shu, X. Cui and Y. Cai, *Nanoscale*, 2025, **17**, 2658–2667.
- Q. Liu, X. Wu, A. H. Coffey, H. Yang, J. Y. Park, Q. Hu, K. Ma, C. Zhu, Y. S. Zhao, L. Dou and K. Wang, *Chem. Commun.*, 2025, **61**, 7644–7647.
- P. Du, Y. Zhao, P. Song, S. Yang, S. Liu, J. Zhang, H. Cai, J. Ni and J. Li, *J. Mater. Sci.: Mater. Electron.*, 2024, **35**, 1870.
- Z. Lu, X. Xu, Y. Gao, Z. Wu, A. Li, Z. Zhan, Y. Qu, Y. Cai, X. Huang, J. Huang, Z. Zhang, T. Luo, L. Peng, P. Liu, T. Shi and W. Xie, *Surf. Interfaces*, 2022, **34**, 102343.
- R. J. D. Tilley, *MRS Bull.*, 2017, **42**, 325.
- D. B. Mitzi, *J. Chem. Soc., Dalton Trans.*, 2001, 1–12, DOI: [10.1039/b007070j](https://doi.org/10.1039/b007070j).
- M. A. Green, A. Ho-Baillie and H. J. Snaith, *Nat. Photonics*, 2014, **8**, 506–514.
- S. Rajukkannu, W. Bunpheng, R. Dhairiyasamy and V. Gopinath, *Sci. Rep.*, 2025, **15**, 833.
- N. K. Elangovan, R. Kannadasan, B. B. Beenarani, M. H. Alsharif, M.-K. Kim and Z. Hasan Inamul, *Energy Rep.*, 2024, **11**, 1171–1190.
- S. Khatoon, S. Kumar Yadav, V. Chakravorty, J. Singh, R. Bahadur Singh, M. S. Hasnain and S. M. M. Hasnain, *Mater. Sci. Energy Technol.*, 2023, **6**, 437–459.
- A. Younis, C.-H. Lin, X. Guan, S. Shahrokhi, C. Y. Huang, W. Yutao, T. He, S. Singh, L. Hu, J. Retamal, J.-H. He and T. Wu, *Adv. Mater.*, 2021, **33**, 2005000.
- Y. Gao, Z. Song, Q. Fu, Y. Chen, L. Yang, Z. Hu, Y. Chen and Y. Liu, *Adv. Mater.*, 2024, **36**, 2405921.
- A. Mahapatra, V. Anilkumar, A. Scarperri, D. J. Kubicki, P. Yadav, M. Mączka and D. Prochowicz, *ACS Photonics*, 2024, **11**, 5091–5099.
- X. Li, S. Aftab, S. Hussain, F. Kabir, A. M. A. Henaish, A. G. Al-Sehemi, M. R. Pallavolu and G. Koyyada, *J. Mater. Chem. A*, 2024, **12**, 4421–4440.
- K. R. Hansen, C. Y. Wong, C. E. McClure, B. Romrell, L. Flannery, D. Powell, K. Garden, A. Berzansky, M. Eggleston, D. J. King, C. M. Shirley, M. C. Beard, W. Nie, A. Schleife, J. S. Colton and L. Whittaker-Brooks, *Matter*, 2023, **6**, 3463–3482.
- Y. Shen, S. Hu, Y. Meng, S. Yip and J. C. Ho, *Mater. Today Electron.*, 2024, **8**, 100100.
- X. Li, J. M. Hoffman and M. G. Kanatzidis, *Chem. Rev.*, 2021, **121**, 2230–2291.
- E. Fransson, J. Wiktor and P. Erhart, *ACS Energy Lett.*, 2024, **9**, 3947–3954.
- R. Lyu, C. E. Moore, T. Liu, Y. Yu and Y. Wu, *J. Am. Chem. Soc.*, 2021, **143**, 12766–12776.
- Y. Mai, J. Tang, H. Meng, X. Li, M. Liu, Z. Chen, P. Zhang and S. Li, *Adv. Compos. Hybrid Mater.*, 2024, **7**, 104.
- E. I. Marchenko, S. A. Fateev, A. A. Petrov, V. V. Korolev, A. Mitrofanov, A. V. Petrov, E. A. Goodilin and A. B. Tarasov, *Chem. Mater.*, 2020, **32**, 7383–7388.
- W. Zhang, J. Zhang, C. Zhang, R. Dong, Y. Xu, Z. Yang, J. Zheng, D. Chen, Q. Liu, W. Yang and M.-H. Shang, *J. Mater. Chem. A*, 2025, **13**, 19670–19681.
- H. A. Chipman, E. I. George and R. E. McCulloch, *arXiv*, 2010, preprint, arXiv:0806.3286, DOI: [10.48550/arXiv.0806.3286](https://doi.org/10.48550/arXiv.0806.3286).
- F. Tavazza, B. DeCost and K. Choudhary, *ACS Omega*, 2021, **6**, 32431–32440.
- Y. Wang and D. L. McDowell, in *Uncertainty Quantification in Multiscale Materials Modeling*, ed. Y. Wang and D. L. McDowell, Woodhead Publishing, 2020, pp. 1–40, DOI: [10.1016/B978-0-08-102941-1.00001-8](https://doi.org/10.1016/B978-0-08-102941-1.00001-8).
- G. Tom, R. J. Hickman, A. Zinzuwadia, A. Mohajeri, B. Sanchez-Lengeling and A. Aspuru-Guzik, *Digital Discovery*, 2023, **2**, 759–774.
- S.-Y. Ding and W. Wang, *Chem. Soc. Rev.*, 2013, **42**, 548–568.
- K. S. Novoselov, A. Mishchenko, A. Carvalho and A. H. Castro Neto, *Science*, 2016, **353**, aac9439.
- P. Xu, X. Ji, M. Li and W. Lu, *npj Comput. Mater.*, 2023, **9**, 42.
- R. Chang, Y.-X. Wang and E. Ertekin, *npj Comput. Mater.*, 2022, **8**, 242.
- Y. Wang, H. Huang, C. Rudin and Y. Shaposhnik, *J. Mach. Learn. Res.*, 2021, **22**, 1–73.
- J. Choi, J. Kim, M. Jeong, B. Park, S. Kim, J. Park and K. Cho, *Small*, 2024, **20**, 2405598.
- P. Liu, X. Li, T. Cai, W. Xing, N. Yang, H. Arandiyani, Z. Shao, S. Wang and S. Liu, *Nano-Micro Lett.*, 2024, **17**, 35.
- S. Bhattacharya and A. Roy, *Comput. Mater. Sci.*, 2024, **231**, 112581.
- L. Lin, T. W. Jones, T. C.-J. Yang, X. Li, C. Wu, Z. Xiao, H. Li, J. Li, J. Qian, L. Lin, J. Q. Shi, S. D. Stranks, G. J. Wilson and X. Wang, *Matter*, 2024, **7**, 38–58.
- J. Li and P. Rinke, *Phys. Rev. B*, 2016, **94**, 045201.
- A. Dunn, Q. Wang, A. Ganose, D. Dopp and A. Jain, *npj Comput. Mater.*, 2020, **6**, 138.
- L. Ward, A. Agrawal, A. Choudhary and C. Wolverton, *npj Comput. Mater.*, 2016, **2**, 16028.



- 41 P. Reiser, M. Neubert, A. Eberhard, L. Torresi, C. Zhou, C. Shao, H. Metni, C. van Hoesel, H. Schopmans, T. Sommer and P. Friederich, *Commun. Mater.*, 2022, **3**, 93.
- 42 L. Breiman, *Mach. Learn.*, 2001, **45**, 5–32.
- 43 J. A. Hanley and B. J. McNeil, *Radiology*, 1982, **143**, 29–36.
- 44 D. Babaian, D. Hill, P. Yu and S. Guha, *J. Mater. Chem. C*, 2025, **13**, 193–202.
- 45 X. Gao, X. Zhang, W. Yin, H. Wang, Y. Hu, Q. Zhang, Z. Shi, V. L. Colvin, W. W. Yu and Y. Zhang, *Adv. Sci.*, 2019, **6**, 1900941.
- 46 K. Fedoruk, S. J. Zelewski, J. K. Zaręba, M. Ptak, M. Mączka and A. Sieradzki, *J. Mater. Chem. C*, 2022, **10**, 10519–10529.
- 47 Z. Yuan, C. Zhou, Y. Tian, Y. Shu, J. Messier, J. C. Wang, L. J. van de Burgt, K. Kountouriotis, Y. Xin, E. Holt, K. Schanze, R. Clark, T. Siegrist and B. Ma, *Nat. Commun.*, 2017, **8**, 14051.
- 48 Y.-Y. Guo, L.-J. Yang and P. Lightfoot, *Crystals*, 2019, **9**, 616.
- 49 S. M. Lundberg and S.-I. Lee, *Adv. Neural Inf. Process. Syst.*, 2017, vol. 30.
- 50 S. Guo, W. Mihalyi-Koch, Y. Mao, X. Li, K. Bu, H. Hong, M. P. Hautzinger, H. Luo, D. Wang, J. Gu, Y. Zhang, D. Zhang, Q. Hu, Y. Ding, W. Yang, Y. Fu, S. Jin and X. Lü, *Nat. Commun.*, 2024, **15**, 3001.
- 51 J. Hu, I. W. H. Oswald, S. J. Stuard, M. M. Nahid, N. Zhou, O. F. Williams, Z. Guo, L. Yan, H. Hu, Z. Chen, X. Xiao, Y. Lin, Z. Yang, J. Huang, A. M. Moran, H. Ade, J. R. Neilson and W. You, *Nat. Commun.*, 2019, **10**, 1276.
- 52 S. Wang, S. Kalyanasundaram, L. Gao, Z. Ling, Z. Zhou, M. Bonn, P. W. M. Blom, H. I. Wang, W. Pisula and T. Marszalek, *Mater. Horiz.*, 2024, **11**, 1177–1187.
- 53 K. Fedoruk-Piskorska, J. K. Zaręba, S. J. Zelewski, A. Gągor, M. Mączka, S. Drobczyński and A. Sieradzki, *ACS Appl. Mater. Interfaces*, 2024, **16**, 28829–28837.
- 54 W. Li, J. He, Y. Zhang, L. Ye, G. Yao, Z. Zhang, S. Li, X. Lu, H. Lu, T. Zeng and Z. Yang, *Cell Rep. Phys. Sci.*, 2025, **6**, 102509.
- 55 B. Settles, *Active Learning Literature Survey*, Technical Report #1648, 2009.
- 56 N. Houlsby, F. Huszár, Z. Ghahramani and M. Lengyel, *arXiv*, 2011, preprint, arXiv:1112.5745, DOI: [10.48550/arXiv.1112.5745](https://doi.org/10.48550/arXiv.1112.5745).
- 57 (a) CCDC 2490415: Experimental Crystal Structure Determination, 2026, DOI: [10.5517/ccdc.csd.cc2plgzzr](https://doi.org/10.5517/ccdc.csd.cc2plgzzr); (b) CCDC 2490430: Experimental Crystal Structure Determination, 2026, DOI: [10.5517/ccdc.csd.cc2plhg8](https://doi.org/10.5517/ccdc.csd.cc2plhg8); (c) CCDC 2490431: Experimental Crystal Structure Determination, 2026, DOI: [10.5517/ccdc.csd.cc2plhh9](https://doi.org/10.5517/ccdc.csd.cc2plhh9).

